

# Semi-Transparent Blade-Coated FAPbBr<sub>3</sub> Perovskite Solar Cells: A Scalable Low-Temperature Manufacturing Process under Ambient Condition

Jessica Barichello, Diego Di Girolamo, Elisa Nonni, Barbara Paci, Amanda Generosi, Minjin Kim, Alexandra Levtchenko, Stefania Cacovich, Aldo Di Carlo, and Fabio Matteocci\*

Perovskite photovoltaics (PVs) is an emerging PV technology that attracts interest thanks to an unprecedented combination of properties, including the ease of the bandgap tunability. The feasibility to deploy wide bandgap absorbers (>2.2 eV) leading to high average visible transmittance (AVT) is particularly intriguing for building-integrated PVs, in particular for smart windows, façades, and agrivoltaics. However, research on this topic is still at the initial stage, especially concerning the development of scalable deposition techniques. Uniform coverage and morphology control of bromide perovskite film are the main issues to tackle. Herein, a systematic study on the development of FAPbBr<sub>3</sub>-based semi-transparent perovskite solar cell (ST-PSC) is presented by replacing spin-coating as the main deposition technique used for the device fabrication. To tackle this topic, the blade coating technique is employed to obtain a manufacturing flow performed at low temperature in the air environment. The results for the blade-coated device show a power conversion efficiency of 5.8%, AVT of 52.3%, and bifacial factor of 86.5%. Moreover, scalable and uniform FAPbBr<sub>3</sub> deposition on 300 cm<sup>2</sup> substrates is presented for the first time. The combination of low temperature, scale-up capability, and air processing along with promising PV performances represent a feasible platform for the future exploitation of PSC in building integrated photovoltaic.

The important metrics for transparent photovoltaics (TPV) are the power conversion efficiency (PCE), the average visible transmittance (AVT), and the color rendering index (CRI). To compare the performance of TPV technologies, light utilization efficiency (LUE) has been introduced by Traverse et al. in 2017.<sup>[2]</sup> In BIPV, Si-based PV technologies are still dominating the market by addressing the demand for visible transparency with the use of spatially segmented opaque c-Si cells without achieving the aesthetical and transparency requirements of a building façade.<sup>[2]</sup> Emergent third-generation PV technologies such as dye-sensitized,<sup>[5]</sup> organic,<sup>[4]</sup> and perovskite<sup>[6,7]</sup> can be potential candidates in the BIPV field. Perovskite solar cells (PSCs) appear as the ideal choice in this respect, owing to the easily tunable bandgap. In fact, by alloying chloride, bromide, and iodide the bandgap of lead perovskites can be continuously tuned from 1.4 eV to above 3 eV.<sup>[7,8]</sup> This property has been mostly investigated in high-efficiency silicon heterojunction


(Si-HJT)/PSC tandem solar cells, implementing a perovskite film with a suitable bandgap (1.65–1.70 eV) overcoming 30% PCE.<sup>[9]</sup> The interest in perovskites with a bandgap wider than 2 eV has been directed mostly to applications alternative to PVs, such as light-emitting devices and photodetectors.<sup>[10,11]</sup> Nonetheless,

## 1. Introduction

Semi-transparent (ST) solar cells have attracted attention due to their promising applications in building integrated photovoltaic (BIPV),<sup>[1,2]</sup> tandem devices,<sup>[3]</sup> and wearable electronics.<sup>[4]</sup>

J. Barichello, D. Di Girolamo, E. Nonni, A. Di Carlo, F. Matteocci  
CHOSE – Centre for Hybrid and Organic Solar Energy  
Department of Electronic Engineering  
University of Rome “Tor Vergata”  
00133 Roma, Italy  
E-mail: fabio.matteocci@uniroma2.it

J. Barichello  
Istituto per i Processi Chimico-Fisici  
IPCF-CNR  
98158 Messina, Italy

 The ORCID identification number(s) for the author(s) of this article can be found under <https://doi.org/10.1002/solr.202200739>.

DOI: 10.1002/solr.202200739

B. Paci, A. Generosi, A. Di Carlo  
ISM-CNR, Istituto di Struttura della Materia, Consiglio Nazionale delle Ricerche  
00133 Roma, Italy

M. Kim, S. Cacovich  
Institut Photovoltaïque d’Île-de-France (IPVF)  
UMR 9006, CNRS  
Ecole Polytechnique  
IP Paris, Chimie Paristech, PSL  
91120 Palaiseau, France

A. Levtchenko  
Institut Photovoltaïque d’Île-de-France (IPVF)  
91120 Palaiseau, France

PCEOs above 10% have been demonstrated by optimizing bromide perovskites (APbBr<sub>3</sub>) in an opaque device stack.<sup>[12]</sup> Bromide perovskites have a bandgap of around 2.3 eV, with a Shockley–Quiesser efficiency limit of around 15% but with a high ceiling for visible transparency.<sup>[13]</sup> Additionally, bromide perovskites comprising a single A-site cation such as methylammonium (MA), formamidinium (FA), and cesium are highly stable in the photoactive phase, different from iodide perovskites.<sup>[14]</sup> Here we selected FAPbBr<sub>3</sub> as a perovskite absorber aiming at the higher thermal stability of FA-based perovskites when compared to MA-based ones.<sup>[15]</sup> Indeed, MAPbX<sub>3</sub> decomposes to gaseous methylamine and hydrogen iodide when exposed to heat and moisture, resulting in loss of optical absorption and severe electron–hole recombination.<sup>[16]</sup> In contrast, the synthesis of FAPbBr<sub>3</sub> is expected to be easier than CsPbBr<sub>3</sub>, for which high temperatures are usually required and the control over the phase purity is challenging.<sup>[17]</sup> Additionally, Zhumekenov et al. reported long carrier diffusion lengths of 19 μm for FaPbBr<sub>3</sub> crystals,<sup>[18]</sup> which are among the largest reported values in halide perovskite materials.

The FAPbBr<sub>3</sub> perovskite having a bandgap of 2.23 eV, reached a maximum of 10% of PCE in opaque devices using SnO<sub>2</sub>/FAPbBr<sub>3</sub>/SpiroOmetad/Gold structure deposited by spin coating deposition.<sup>[19]</sup> Grancini et al. studied the beneficial introduction of Cs<sup>+</sup> cation in FAPbBr<sub>3</sub> deposited by spin coating deposition<sup>[20]</sup> while Ying et al. focused on moving the FAPbBr<sub>3</sub> deposition from spin to blade coating with the aim of scaling up the deposition area (>1 cm<sup>2</sup>).<sup>[21]</sup> The best results showed a PCE of 7.29% using opaque high-temperature processed FTO/TiO<sub>2</sub>/FAPbBr<sub>3</sub>/Spiro-OMeTAD/Au device stack. By replacing the gold with silver nanowires, the PCE decreased to 5.25% showing AVT of 25% and LUE of 1.31%. FAPbBr<sub>3</sub> has been also used for PIN devices deposited by spin coating deposition reaching a maximum PCE of 5.71%, AVT of 35%, and LUE of 1.99.<sup>[22]</sup> The blade coating method is successfully known for its numerous advantages in comparison to spin coating.<sup>[23]</sup> Indeed, while the spin coating is a well-established deposition method for small-area cells, solvent evaporation, and the kinetics of crystallization growth during the deposition become critical as the active area increases.<sup>[24]</sup> In contrast, the control of morphology/quality of the film is quite challenging if compared to spin coating.<sup>[23,24]</sup>

In this work, we present a systematic study of the fabrication process of highly transparent devices based on the ITO/SnO<sub>2</sub>/FAPbBr<sub>3</sub>/PTAA/ITO device stack. We selected SnO<sub>2</sub> and PTAA as the electron transport layer (ETL) and hole transport layer (HTL), respectively, to limit the processing temperature below 100 °C, permitting us to extend the fabrication procedure discussed in this work to flexible plastic substrates.<sup>[25]</sup> SnO<sub>2</sub> has been deemed as an ideal ETL due to high carrier mobility, low parasitic absorbance in the visible spectrum, high chemical stability, and insensitivity to ultraviolet (UV) light.<sup>[26]</sup> The PTAA polymer has been tested in both NIP and PIN device architecture showing great potential in terms of PV performance,<sup>[27]</sup> long-term stability,<sup>[28]</sup> and tolerance to sputtering damage.<sup>[29]</sup> We consider several fabrication processes from fully spin-coated (SC) to fully blade-coated (BC) devices. For SC samples, we obtained a maximum PCE of 8.11% and AVT of 47.4% corresponding to an LUE equal to 3.8 which represents one of the higher PCE in the literature for FAPbBr<sub>3</sub>-based devices made at low-temperature processing. For fully BC devices, we replaced

the SC technique with BC for all the constituent layers forming the stack (SnO<sub>2</sub>, FAPbBr<sub>3</sub>, and PTAA) reaching PCE equal to 5.8%, AVT of 52.3%, and LUE equal to 3. Moreover, the fully BC device demonstrated a bifaciality factor of 86.5% (defined as PCE<sub>rear</sub>/PCE<sub>front</sub>), a remarkably high value if compared to those shown in the literature.<sup>[30,31]</sup> Bifacial solar cells are able to collect photons from the incident and albedo radiation reaching both the front side and rear side of a solar module, which is highly interesting for the Agrivoltaics field.<sup>[32]</sup> Finally, we demonstrated the uniformity and the photoluminescence (PL) stability of the FAPbBr<sub>3</sub> at 100 cm<sup>2</sup>-sized substrates by performing spatial PL maps for future applications on perovskite solar modules.

## 2. Results and Discussion

Semi-transparent PSCs (ST-PSCs) have been fabricated using a planar N–I–P architecture consisting of the following stack: ITO/SnO<sub>2</sub>/FAPbBr<sub>3</sub>/PTAA/ITO. The entire fabrication process is performed at low temperature (<100 °C). The final goal of this work is to demonstrate a fully BC device by gradually replacing the spin coating technique for the deposition of the constituent layers. In **Figure 1**, we show the sample types investigated in this work, hereafter named Sample A, Sample B, Sample C, and Sample D. Samples A and B are fabricated using SC FAPbBr<sub>3</sub> perovskite by replacing the SC (Sample A) with BC (Sample B) for SnO<sub>2</sub> layer. On the contrary, Samples C and D are based on BC FAPbBr<sub>3</sub> perovskite by replacing the SC (Sample C) with BC (Sample D) for the PTAA layer. Samples A and D represent Fully SC and BC devices, respectively. The icons clarified the deposition technique used for the deposition of each layer (SnO<sub>2</sub>, FAPbBr<sub>3</sub>, and PTAA) of each sample type.

In **Figure 2**, we report the results of the investigation on structural and morphological properties of the FAPbBr<sub>3</sub> perovskite deposited by varying the deposition technique and method (Sample A vs Sample D) are reported in Figure 2. X-ray diffraction (XRD in Figure 2a), shows peaks attributed to ITO accordingly to JCPDS card number 32-0458 are highlighted. FAPbBr<sub>3</sub> reflections are labeled according to the literature and the patterns perfectly match the perovskite pure α-phase for both samples.<sup>[10,33]</sup> Despite having similar quality in terms of crystallinity, it is noticeable that *h*00 orientation is relatively more privileged in the BC film. In fact, the ratio of the integrated intensities between the peaks (100), (200), and (300) to those indexed as (210) and (211) is significantly higher for the BC sample. The possibility to manipulate the texture of the perovskite thin film by modifying the deposition method (spin coating vs blade coating) and the crystallization technique (solvent quenching method vs. sequential deposition), also reported in the literature,<sup>[34]</sup> is an interesting finding aiming at future investigation and exploitation of the (eventual) anisotropy of FAPbBr<sub>3</sub> perovskite thin films optoelectronic properties.

Notably, BC perovskite has been obtained starting from CsBr-doped PbBr<sub>2</sub> that helps to solubilize the PbBr<sub>2</sub> in DMSO avoiding the formation of needle-like crystal after storage (Figure S2, Supporting Information). We speculate that the small amount of CsBr-doping (less than 3% in molar ratio) is not contributing to structural changes on the final FAPbBr<sub>3</sub> perovskite as confirmed by XRD diffractograms in Figure 2a.

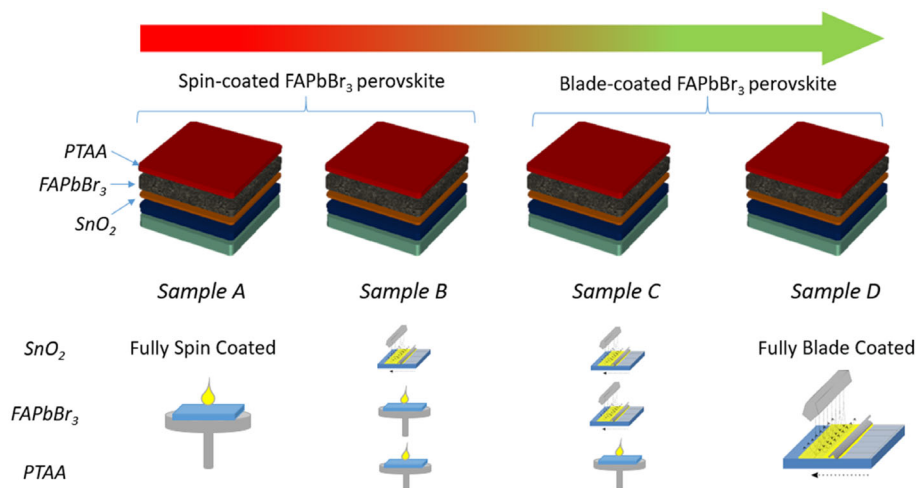


**Figure 1.** Device structures optimized in this work based on Glass-ITO/SnO<sub>2</sub>/FAPbBr<sub>3</sub>/PTAA/ITO: Replacement of spin coating with blade coating of each layer forming the device stack.

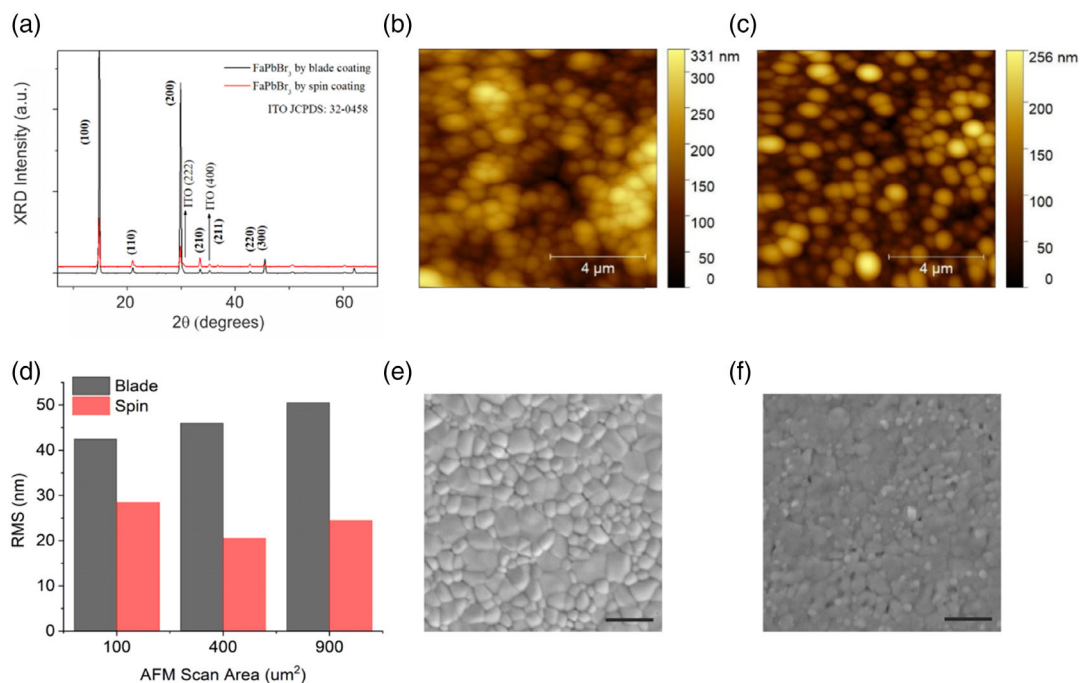


**Figure 2.** a) X-ray diffraction (XRD) patterns of spin-coated (SC, red line) and blade-coated (BC, black line) FAPbBr<sub>3</sub> on ITO/SnO<sub>2</sub>/FAPbBr<sub>3</sub> samples. Each diffraction peak is associated with the crystalline layers (perovskite and ITO). b,c) Atomic force microscope (AFM) images of the FAPbBr<sub>3</sub> films with an AFM scan area of 100 μm<sup>2</sup>, collected for: b) the SC and c) BC FAPbBr<sub>3</sub> films. d) Root mean square (RMS) roughness measured by AFM images with different scan areas (100, 400, 900 μm<sup>2</sup>) for SC and BC films. e,f) Planar scanning electron microscope (SEM) images of the FAPbBr<sub>3</sub> films deposited by: e) SC and f) BC. The scale bar is 2 μm for both SEM images.

Atomic force microscope (AFM) images (Figure 2b,c and S3, Supporting Information) at 10 × 10 μm<sup>2</sup> were collected upon different surface portions for each sample and a statistical (Figure 2d) analysis was performed to observe the surface roughness evolution as a function of the different deposition methods. The surface roughness of the SC and BC FAPbBr<sub>3</sub> perovskites are markedly different where the SC perovskite displays a lower

RMS roughness (20–30 nm) with respect to the BC perovskite (40–50 nm) for all the AFM scan areas (100, 400, 900 μm<sup>2</sup>).

Planar SEM images (Figure 2e,f) show the morphology of the perovskite layers in good agreement with those reported in AFM measurements. We can notice, for both deposition methods, the presence of μm-scale size grains interconnected with each other with smaller sub-micrometer size grains. However, SC

perovskite does not present pin-holes at the grain boundaries if compared with BC perovskite as expected from the lower surface roughness. This aspect becomes even more relevant if considered the successive deposition of PTAA polymer with an extremely low film thickness of around 30 nm.

The first step toward a fully BC device stack is the deposition of the SnO<sub>2</sub> as ETL. For the optimization of the BC SnO<sub>2</sub> layer (Sample B), we fabricated 0.4 cm<sup>2</sup>-sized ST-PSC by varying the dilution of the SnO<sub>2</sub> nanoparticle (np-SnO<sub>2</sub>) dispersion in deionized (DI) water. For the SC devices (Sample A), we fixed the dilution (1:5 volume ratio) in DI water of the np-SnO<sub>2</sub> ink.<sup>[35]</sup> For Sample B, we evaluated three different dilutions (1:5, 1:3, No dilution) fabricating batches of 32 devices for each. In **Figure 3**, we report the statistical dispersion of the PCE results using the three different dilutions of the np-SnO<sub>2</sub> inks. The results show the presence of a not negligible number of cells (hereafter called “dead cells”) with low PCE (<2%), mainly ascribed to shunting issues (low V<sub>oc</sub>). The number of “dead cells” remarkably decreased at low dilutions (1:3 and No dilution) of the np-SnO<sub>2</sub> ink being equal to 18, 10, 8. This is mainly related to the enhanced coverage of the SnO<sub>2</sub> layer at low dilution avoiding shunting paths at the SnO<sub>2</sub>/FAPbBr<sub>3</sub> interface.<sup>[36]</sup> It is important to note that 1:5 dilution experienced a lack of reproducible results for both SC (Sample A) and BC (Sample B) showing 50% and 56% of dead cells in the batch, respectively.

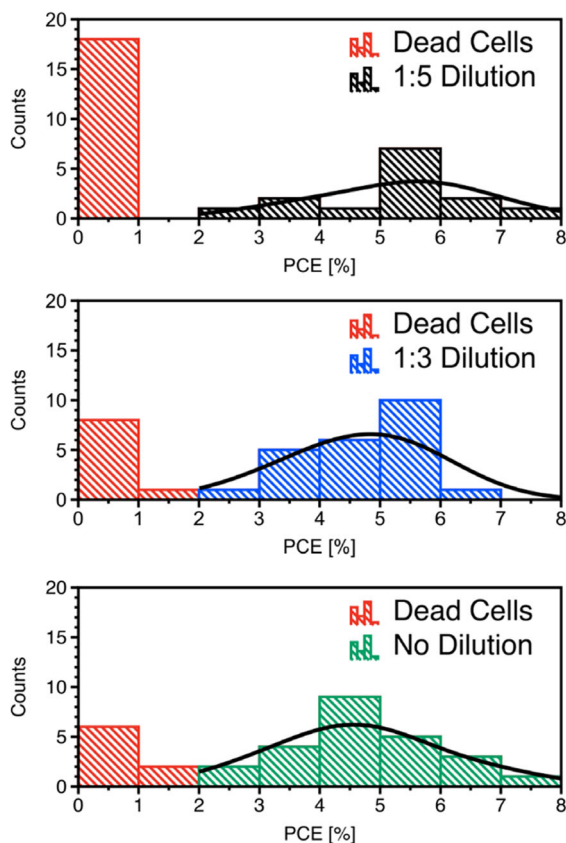


**Figure 3.** Normal distribution of the power conversion efficiency (PCE) results obtained on a batch of 32 semi-transparent perovskite solar cell (ST-PSC) devices for each dilution of the SnO<sub>2</sub> nanoparticle ink: No dilution, 1:3 SnO<sub>2</sub>: water; 1:5 SnO<sub>2</sub>: water.

For working cells, the PCE results are reported as a normal distribution ranging from 2% to 8% showing the following average values for the three tested dilutions: 24 for no dilution, 23 for 1:3, and 14 for 1:5. With aim of improving the reproducibility of the results, we found the best compromise between reproducibility and PCE results using 1:3 dilution, leading to an average PCE of 4.65%. In Figure S4, Supporting Information, the optimized BC SnO<sub>2</sub> layer was further characterized by AFM to evaluate the morphology, surface coverage, and roughness of the layer. The results show an extremely homogeneous and smooth surface with a roughness of around 1 nm acquired at different surface areas.

In **Figure 4a**, we report the statistical distribution of PCE results obtained for the different samples (A, B, C, and D) introduced in Figure 1. The *J*-*V* characteristics and maximum power point tracking (MPPT) for tested cells are also reported in Figure S5, Supporting Information. The average PV parameters (V<sub>oc</sub>, J<sub>sc</sub>, FF, PCE) are reported in Table S1, Supporting Information. PCE results do not change significantly comparing the SnO<sub>2</sub> layers deposited by SC (Sample A) and BC (Sample B) with average PCE of 7.1% and 6.7%, respectively, thanks to the optimization of the SnO<sub>2</sub> nanoparticle ink. The PCE comparison of ST-PSC based on the perovskite layer made by SC and BC (highlighted in Figure 4a), Sample B and Sample C, respectively, show a remarkable decrease of the PCE mainly attributed to decrease in J<sub>sc</sub> showing 7.9 and 6.4 mA cm<sup>-2</sup>, respectively. The discrepancy in J<sub>sc</sub> is mainly due to the lower FAPbBr<sub>3</sub> perovskite thickness obtained for BC Sample C with respect to SC sample B being equal to 200 and 350 nm, respectively (see Figure S6, Supporting Information). This is also evident by comparing the incident photon-to-current efficiency (IPCE) spectra of the two cells as reported in Figure 4b where the IPCE decrease in the range of wavelengths from 380 to 530 nm is related to the lower light absorption of Sample C. On the opposite, the BC of PTAA (Sample D) introduces only a small reduction of PCE and IPCE. The BC deposition of thicker FAPbBr<sub>3</sub> layers (~400 nm) is challenging due to the lack of control over the perovskite crystallization and growth. In Figure S7, Supporting Information, we reported the planar SEM images of the FAPbBr<sub>3</sub> obtained by increasing the film thickness. The presence of perovskite cuboids at the film surface leads to haze and rougher films. The analysis of the UV-visible transmittance allows us to link the lower current generation to the lower light harvesting from BC perovskites. In fact, the transmittance of SC perovskites attains a low value below 10% at the band edge (around 540 nm) while the one from BC perovskites remains around 20%. The difference of 15% in transmittance in the range between 400 and 550 nm closely fits the one in IPCE. Notably, the lower light absorption enhances the AVT of BC devices up to 52%, above the 47% from SC devices as shown in Figure 4c. To compare the SC and BC deposition at the same thickness, we lowered the thickness of the SC FAPbBr<sub>3</sub> perovskite by reducing the SC solution concentration from 1.4 to 1.1 M. The *J*-*V* results show the following PV parameters: V<sub>oc</sub> = 1.44 V, J<sub>sc</sub> = 6.94 mA cm<sup>-2</sup>, FF = 64.7%, PCE = 6.5%. Finally, the BC of the PTAA polymer was optimized in Sample D by varying the coating speed from 5 to 100 mm s<sup>-1</sup> to replace the layer with SC. In Figure S8, Supporting Information, the transmittance spectra of the ITO/PTAA samples deposited by varying the BC speed and compared with

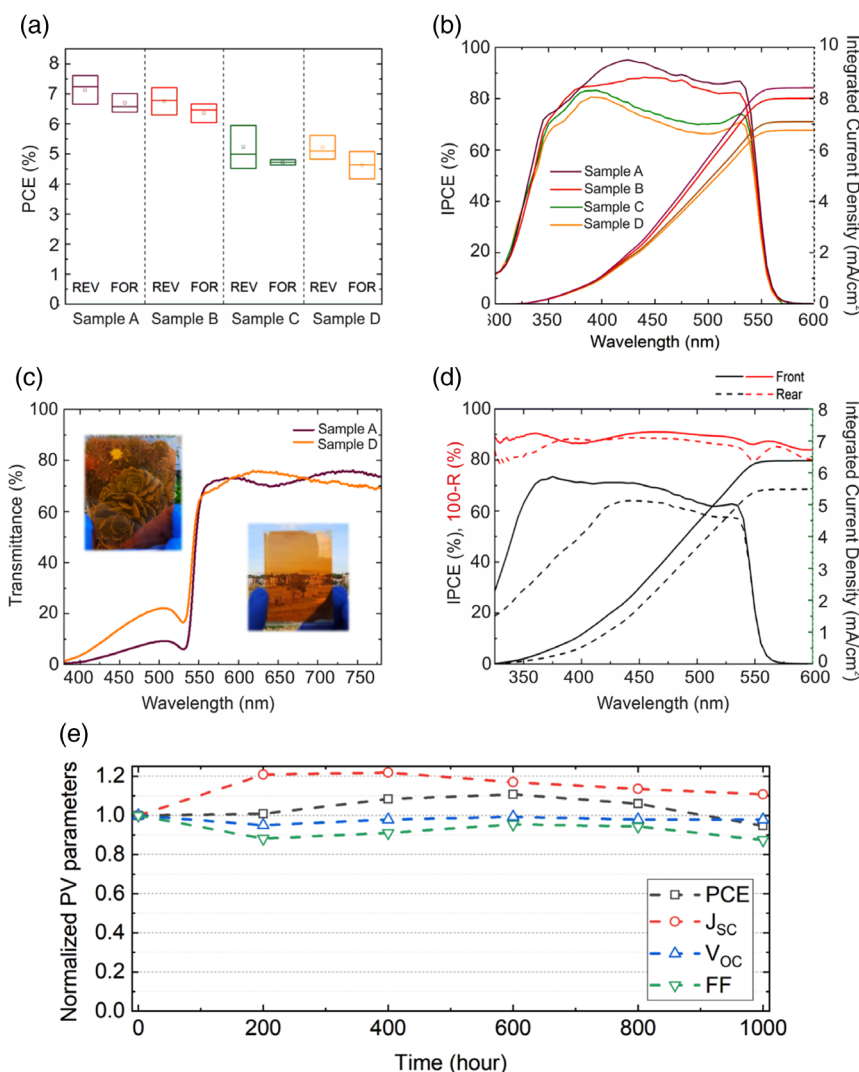


**Figure 4.** a) Statistical power conversion efficiency (PCE) results obtained on a batch of six devices for each device stack structure by measuring at 1 Sun AM1.5G illumination condition under reverse and forward scan directions. b) IPCE spectra and integrated currents of the ST-PSC devices following the device stack shown in Figure 1. c) Representative transmittance spectra obtained for Sample A (fullySC) and Sample D (fullyBC) device stacks and d) incident photon-to-current efficiency (IPCE) and 100-R spectra measured by illuminating from the front (solid lines) and rear side (dashed lines) in Sample D. e) Normalized photovoltaic (PV) parameters measured during dry heat test at 85 °C in air by following ISOS-D2 stability protocol.

SC PTAA sample deposited at the same concentration. From the results,  $100 \text{ mm s}^{-1}$  was chosen as the BC speed for device fabrication.

The metrics for TPV devices ( $J$ - $V$  parameters, AVT, and LUE) for champion devices are reported in **Table 1**. Notably, the LUE parameter was greater than 3% in a fully BC device (Sample D) showing the good potential of the developed process for ST-PSCs if compared to the other transparent PV technologies.<sup>[2]</sup>

An important feature of a ST PV field is the bifacial illumination: a strategy to increase the output of the PV system working with the reflected light from the ground. In Sample D, we measured the PV performance illuminating the device from the front (glass-SnO<sub>2</sub>-Perovskite-PTAA-ITO) and rear side (ITO-PTAA-Perovskite-SnO<sub>2</sub>-glass) reaching 5.1% and 4.4%, respectively (Table S2, Supporting Information). A remarkably high

bifaciality factor of 86.5% was obtained if compared with results reported in the literature.<sup>[31,37]</sup> In Figure 4d, we reported the IPCE spectra by varying the illumination side in Sample D device. The results showed lower IPCE and integrated current density in rear side illumination due to the reflection of the sputtered ITO electrode and the parasitic absorbance of the PTAA layer. A higher reflectance illuminating from the air/sputtered-ITO interface is measured in comparison with air/glass/commercial-ITO (front) interface. To demonstrate this, we plot the 100-R spectra by varying the illumination side showing higher reflectance in the entire range of wavelengths corresponding to current losses of about  $0.3 \text{ mA cm}^{-2}$ . Moreover, the parasitic absorption of the PTAA contributed to current losses of about  $0.4 \text{ mA cm}^{-2}$ . In Figure 4e, we reported the results of the dry heat stability test performed on Sample D device

**Table 1.** PV parameters of champion ST-PSC cells for each structure.

Sample	Scan	$V_{oc}$ [V]	FF [%]	$J_{sc}$ [ $\text{mA cm}^{-2}$ ]	Integrated $J_{sc}$ [ $\text{mA cm}^{-2}$ ]	PCE [%]	AVT [%]	LUE [%]
Sample A	Reverse	1.44	67.0	-8.3	-8.4	8.0	47	3.8
	Forward	1.43	73.6	-7.7		8.1		
Sample B	Reverse	1.45	61.1	-8.2	-8.0	7.3		
	Forward	1.44	53.8	-8.3		6.5		
Sample C	Reverse	1.43	68.3	-6.1	-7.0	6.0		
	Forward	1.42	51.3	-6.5		4.7		
Sample D	Reverse	1.41	58.0	-7.0	-6.8	5.8	52	3.0
	Forward	1.40	52.1	-6.5		4.8		

following the ISOS-D2 protocol for 1000 h.<sup>[38]</sup> The not-encapsulated ST-PSC cell was stored in an oven at 85 °C in air and measured during the aging time (200, 400, 600, 800, and 1000 h). Interestingly, the device retained 95% of the initial PCE value without suffering any degradation. This is due to the presence of sputtered ITO top contact that efficiently works also as encapsulating material preserving the cell from moisture-driven degradation.

To exploit the spatial uniformity of BC stack, we prepared ITO/SnO<sub>2</sub>/FAPbBr<sub>3</sub> and ITO/SnO<sub>2</sub>/FAPbBr<sub>3</sub>/PTAA stacks on 12 × 10 cm<sup>2</sup> (Figure 5a) sized substrates, then cut to 10 × 10 cm<sup>2</sup> (Figure 5b) to perform PL analysis. The FAPbBr<sub>3</sub> deposition was performed by employing a dipping process in the second step of

the sequential deposition that might influence the thin film uniformity. We characterized the 10 × 10 cm<sup>2</sup> samples by employing a hyperspectral photoluminescence imaging system. Such a technique allows to acquire 3D datasets { $x, y, \lambda$ }, with two dimensions being spatial and the third one representing PL intensity ( $I_{PL}$ ) as a function of the wavelength. Therefore, each pixel of the measured image contains  $I_{PL}$  versus wavelength ( $\lambda$ ) information. Importantly, this method is contactless, hence it can be used at any step of device fabrication, allowing to probe the optoelectronic properties not only of full devices but also of half stacks or bare absorbers.<sup>[39]</sup> Here, we observe a good coverage over the whole surface of the sample for both half stack (ITO/SnO<sub>2</sub>/FAPbBr<sub>3</sub>) and full stack (ITO/SnO<sub>2</sub>/FAPbBr<sub>3</sub>/PTAA),

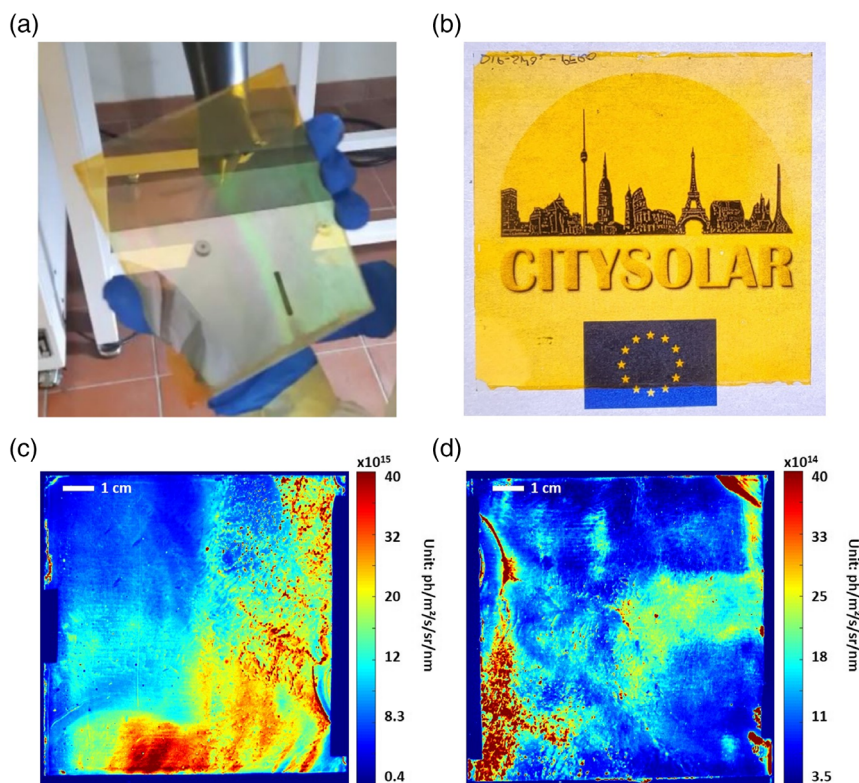


**Figure 5.** a) ST FAPbBr<sub>3</sub> sample before cutting (12 × 10 cm<sup>2</sup>), b) a 10 × 10 cm<sup>2</sup> sample cut to fit the PL imaging system, c)  $I_{PL-max}$  maps of ITO/SnO<sub>2</sub>/FAPbBr<sub>3</sub>, and d) ITO/SnO<sub>2</sub>/FAPbBr<sub>3</sub>/PTAA architectures.

as shown in the PL maximal intensity ( $I_{\text{PL-max}}$ ) maps reported in Figure 5c,d respectively. However, we can observe the presence of not completely homogenous zones, which might be ascribed to the local variation of the absorber thickness. The upscaling process has still not been fully optimized and it will be the subject of future work. Full PL spectra and photoluminescence emission peak maps are shown in Figure S9, Supporting Information. By comparing half and full stack we can observe a tenfold reduction of the  $I_{\text{PL-max}}$ , which varies from  $1.6297e^{+16}$  to  $1.2962e^{+15}$   $\text{ph m}^{-2} \text{s}^{-1} \text{sr}^{-1} \text{nm}^{-1}$  (median values). The drop of PL intensity after the deposition of the HTL in steady-state PL measurements indicates the presence of non-radiative recombination at the interface between the absorber and HTL.<sup>[40]</sup> Moreover, it is worth noting that on full stacks the  $I_{\text{PL-max}}$  has maintained a good uniformity, revealing that PTAA deposition by blade coating resulted in a homogenous coverage of the perovskite thin film. Finally, we further demonstrated the scalability of the process by replacing the dip coating with blade coating of FAPbBr<sub>3</sub> solution on a  $15 \times 20 \text{ cm}^2$ -sized substrate. In Figure S10, Supporting Information, we resume the manufacturing process of fully BC FAPbBr<sub>3</sub> perovskite. XRD characterization confirmed the structural properties of the FAPbBr<sub>3</sub> perovskite shown in Figure 2a for Dip-coated samples (Figure S11, Supporting Information).  $I_{\text{PL-max}}$  maps of ITO/SnO<sub>2</sub>/FAPbBr<sub>3</sub> on a  $10 \times 10 \text{ cm}^2$ -sized substrate revealed good uniformity of the fully BC FAPbBr<sub>3</sub> perovskite (Figure S12, Supporting Information).

### 3. Conclusion

The present study aims to develop a scalable manufacturing process for large-area ST perovskite-based devices in an air environment and at low temperatures ( $\leq 100^\circ\text{C}$ ). The development of an up-scaling process entirely performed in air using scalable techniques at low-temperature processing appears crucial going toward a future industrialization. Moreover, the semi-transparency of the device is vital to exploit perovskite technologies in the BIPV field and indoor environment. In this work, we have shown how the blade-coating represents a potential candidate for replacing spin-coating as the main deposition technique used for the fabrication of ST-PSC using bromide perovskite. First, we demonstrated state-of-the-art ST-PSC entirely made by spin-coating reaching PCE and AVT values equal to 8.11% and 47%, respectively. Then, we developed a blade-coating process for each layer forming the device stack (SnO<sub>2</sub>, FAPbBr<sub>3</sub>, and PTAA). Interestingly, fully BC ST-PSC shows a maximum PCE of 5.8%, AVT equal to 52%, and a bifaciality factor of 86.5%. The optimization of the FAPbBr<sub>3</sub> perovskite deposition was corroborated by a thorough structural and morphology investigation based on XRD, SEM, and AFM. Preliminary results on thermal stability are also encouraging for fully BC devices that showed negligible impact on PV performance after storage at  $85^\circ\text{C}$  for 1000 h. The spatial uniformity of the BC FAPbBr<sub>3</sub> perovskite on a large  $10 \times 10 \text{ cm}^2$  size substrate is evaluated by measuring PL signal using a hyperspectral imaging system. This work opens the via for the future development of ST large-area perovskite solar modules.

### 4. Experimental Section

**Device Fabrication:** ITO glass substrates (Kintec company,  $10 \Omega \square^{-1}$  as sheet resistance) were etched using a nanosecond UV laser to obtain the desired layout consisting of four small cells with an active area of  $0.4 \text{ cm}^2$  on  $2.5 \times 2.5 \text{ cm}^2$  sized substrate (Figure S1, Supporting Information). For Samples B, C, and D, ITO glass substrates were etched to obtain sixteen cells on  $5 \times 7 \text{ cm}^2$  sized substrates. Then, the samples were rinsed in deionized water/soap solution and washed with deionized water to remove the residual soap. Afterward, the samples were cleaned in an ultrasonic bath by soaking them subsequently in deionized water and 2-propanol for 10 min. Prior to the SnO<sub>2</sub> deposition, UV-ozone treatment was performed for 10 min. For Sample A, the SnO<sub>2</sub> nanoparticle ink was prepared by diluting the commercial SnO<sub>2</sub> dispersion (Alfa Aesar) with deionized water at a 1:5 volume ratio. The diluted SnO<sub>2</sub> dispersion is deposited by spin coating at 2500 rpm for 40 s and then the samples are annealed at  $100^\circ\text{C}$  for 10 min. For Sample B, the SnO<sub>2</sub> nanoparticle ink was prepared by varying the dilution in deionized water. No dilution, 1:3 v/v%, 1:5 v/v% were tested using the BC technique (blade height:  $70 \mu\text{m}$ ,  $25 \mu\text{L}$  of solution,  $100^\circ\text{C}$  as annealing temperature, speed:  $10 \text{ mm s}^{-1}$ , No airflow). For Samples C and D, we repeated the same process using 1:3 v/v% dilution.

For Samples A and B, a stoichiometric perovskite solution (FAPbBr<sub>3</sub>) was prepared by mixing 1.4 M PbBr<sub>2</sub> and 1.4 M FaBr in DMSO solvent. Then, the FAPbBr<sub>3</sub> perovskite film was deposited by spin coating at 4000 rpm for 20 s using the solvent quenching method. After 10 s,  $200 \mu\text{L}$  of ethyl acetate was dropped on the surface of the samples to induce perovskite crystallization. The samples are then annealed at  $80^\circ\text{C}$  for 10 min. For Samples C and D, the FAPbBr<sub>3</sub> perovskite film was deposited by air-flow assisted blade coating using the sequential deposition method (Figure S1, Supporting Information). During the first step, a solution of 1.4 M of PbBr<sub>2</sub> doped with  $10 \text{ mg mL}^{-1}$  of CsBr in DMSO was prepared. Then, the CsBr doped PbBr<sub>2</sub> layer was deposited by air-flow assisted blade coating at  $60^\circ\text{C}$  (blade height:  $70 \mu\text{m}$ ,  $25 \mu\text{L}$  of solution,  $100^\circ\text{C}$  as annealing temperature, speed:  $5 \text{ mm s}^{-1}$ , air flow rate:  $250 \text{ L min}^{-1}$ , air temperature: RT). The FAPbBr<sub>3</sub> layer is then obtained by dipping the samples in FAPbBr<sub>3</sub> solution ( $10 \text{ mg mL}^{-1}$  in 2-propanol) for 10 min. Alternatively, the FAPbBr<sub>3</sub> layer can be obtained by replacing the dip coating with blade coating depositing FAPbBr<sub>3</sub> solution at  $60^\circ\text{C}$  with the following parameters (blade height:  $70 \mu\text{m}$ ,  $25 \mu\text{L}$  of the solution, speed:  $5 \text{ mm s}^{-1}$ , No Airflow).

Doped PTAA solution ( $10 \text{ mg mL}^{-1}$ , 10 kDa) in toluene was prepared by adding into the pristine solution  $10 \mu\text{L mL}^{-1}$  of 4-*tert*-butylpyridine and  $5 \mu\text{L mL}^{-1}$  of LiTFSI stock solution ( $170 \text{ mg mL}^{-1}$  in acetonitrile). For Samples A, B, and C, the PTAA layer was obtained by spin coating at 4000 rpm for 20 s. For Sample D, the PTAA layer was obtained by blade coating at RT (blade height:  $70 \mu\text{m}$ ,  $25 \mu\text{L}$  of solution, speed:  $100 \text{ mm s}^{-1}$ , No Airflow). Low-temperature ITO deposition was performed by magnetron sputtering at  $1.1 \times 10^{-3}$  mBar and 60 W RF power using an industrial in-line magnetron sputtering (KENOSISTEC S.R.L., KS 400 In-Line). Inert Ar gas is purged in the chamber (40sccm) during the ITO deposition to activate the Ar<sup>+</sup> plasma. The sample holder is moved below the ITO cathode with  $120 \text{ cm min}^{-1}$  speed for 300 cycles to achieve the 100 nm thick ITO film. The sheet resistance of the sputtered ITO top contact is equal to  $30 \Omega \square^{-1}$ .

XRD: A Panalytical Empyrean X-ray diffractometer was used to perform XRD measurements in Bragg-Brentano configuration. Detection was accomplished by means of a PixCel 3D detector working in linear mode and a Cu-anode X-ray tube (K-Alpha1 [ $\lambda$ ] = 1.54060; K-Alpha2 [ $\lambda$ ] = 1.54443) was used as the source. Incident optical pathway was set by divergent slits (Divergence Slit Type Fixed, Divergence Slit Size [ $^\circ$ ] = 0.2177) and patterns were collected in the  $5^\circ < 2\theta < 70^\circ$  angular range (Gonio acquisition, Step Size [ $^\circ 2\theta$ ] = 0.0260, Scan Step Time [s] = 1145, Scan Type Continuous). Samples were located onto a flat sample holder for thin films and generator parameters were kept fixed at 45 mA and 40 kV.

AFM: An in-house developed AFM mounting a  $30 \mu\text{m} \times 30 \mu\text{m}$  scanner was used to determine the morphological surface characteristics of the

various samples. Non-contact mode acquisitions were collected upon several portions of each film by means of aluminum-coated standard tapping AFM probes (Nanosensors), combining high operation stability with outstanding sensitivity and fast scanning ability. Images ranging from  $30 \times 30$  to  $10 \times 10 \mu\text{m}^2$  (500 points/image) were collected.

**SEM:** SEM measurements were performed using a high-resolution SEM with FEG Schottky electron source (TESCAN MIRA).

**Hyperspectral Photoluminescence Imaging:** Macro view ( $\approx 10$  cm scale) hyperspectral photoluminescence images were acquired with Grand-EOS equipment from Photon etc. A wide-field illuminating blue LED system (Ucube 405 nm, from UWAVE), homogeneously brightens specimens at a power of one Sun on the stage. All PL measurements were performed in an ambient atmosphere at room temperature without humidity control in the clean room. In this environment, complete reproducibility of PL acquisitions was achieved.

**PV Performance:** Current density–voltage ( $J$ – $V$ ) characteristic of devices were acquired in air using a solar simulator (ABET Sun 2000, class A) calibrated at AM 1.5 and  $100 \text{ mW cm}^{-2}$  illumination condition using a certified reference Si Cell (RERA Solutions RR-1002). The  $J$ – $V$  characteristics were acquired in both scan directions (reverse and forward) using a scan rate of  $300 \text{ mV s}^{-1}$  and step voltage of 50 mV. A commercial setup of a 4-wire source meter and several channels (Arko-Ariadne, Cicci Research srl) was utilized. IPCE spectra were acquired using a commercial setup (Arko-Adriane, Cicci Research srl) based on a 300 W xenon lamp, able to acquire a spectrum from 300 to 1100 nm with a resolution of 2 nm. AVT values were calculated using Equation (1), Supporting Information.

## Supporting Information

Supporting Information is available from the Wiley Online Library or from the author.

## Acknowledgements

This project has received funding from the European Union's Horizon 2020 research and innovation programme under Grant Agreement No 101007084 (CITYSOLAR). A.L. thanks the French Government in the frame of the program of investments for the future (Programme d'Investissement d'Avenir ANR-IEED-002-01).

## Conflict of Interest

The authors declare no conflict of interest.

## Data Availability Statement

The data that support the findings of this study are available from the corresponding author upon reasonable request.

## Keywords

building integrated photovoltaics, low-temperature processing, perovskite solar cells, tandem, transparent photovoltaics

Received: August 11, 2022

Revised: October 25, 2022

Published online: December 20, 2022

[1] W. Wu, H. M. Skye, *Renewable Sustainable Energy Rev.* **2021**, *142*, 110859.

[2] C. J. Traverse, R. Pandey, M. C. Barr, R. R. Lunt, *Nat. Energy* **2017**, *2*, 849.

- [3] a) P. Tockhorn, J. Sutter, A. Cruz, P. Wagner, K. Jäger, D. Yoo, F. Lang, M. Grischek, B. Li, A. Al-Ashouri, E. Köhnen, M. Stollerfoht, D. Neher, R. Schlattmann, B. Rech, B. Stannowski, S. Albrecht, C. Becker, Research Square, **2022**; b) D. Rossi, K. Forberich, F. Matteocci, M. Auf der Maur, H.-J. Egelhaaf, C. J. Brabec, A. Di Carlo, *Sol. RRL* **2022**, *6*, 2200242; c) L. Zuo, X. Shi, W. Fu, A. K. Y. Jen, *Adv. Mater.* **2019**, *31*, 1901683.
- [4] a) J. Krantz, T. Stubhan, M. Richter, S. Spallek, I. Litzov, G. J. Matt, E. Spiecker, C. J. Brabec, *Adv. Funct. Mater.* **2013**, *23*, 1711; b) Q. Xue, R. Xia, C. J. Brabec, H. L. Yip, *Energy Environ. Sci.* **2018**, *11*, 1688; c) X. Wang, J. Wang, J. Han, D. Huang, P. Wang, L. Zhou, C. Yang, X. Bao, R. Yang, *Nano Energy* **2021**, *81*, 105612.
- [5] a) A. Hagfeldt, G. Boschloo, L. Sun, L. Kloo, H. Pettersson, *Chem. Rev.* **2010**, *110*, 6595; b) D. Colonna, S. Colodrero, H. Lindström, A. Di Carlo, H. Míguez, *Energy Environ. Sci.* **2012**, *5*, 8238; c) P. Mariani, L. Vesce, A. Di Carlo, *Semicond. Sci. Technol.* **2015**, *30*, 104003; d) W. Naim, V. Novelli, I. Nikolinos, N. Barbero, I. Dzeba, F. Grifoni, Y. Ren, T. Alnasser, A. Velardo, R. Borrelli, S. Haacke, S. M. Zakeeruddin, M. Graetzel, C. Barolo, F. Sauvage, *JACS Au* **2021**, *1*, 409.
- [6] a) A. Singh, F. Matteocci, H. Zhu, D. Rossi, S. Mejaouri, S. Cacovich, M. Auf Der Maur, F. Sauvage, A. Gagliardi, M. Grätzel, A. Di Carlo, *Sol. RRL* **2021**, *5*, 2100277; b) B. Shi, L. Duan, Y. Zhao, J. Luo, X. Zhang, *Adv. Mater.* **2020**, *32*, 1806474.
- [7] F. Matteocci, D. Rossi, L. A. Castriotta, D. Ory, S. Mejaouri, M. A. der Maur, F. Sauvage, S. Cacovich, A. Di Carlo, *Nano Energy* **2022**, *101*, 107560.
- [8] a) T. Jesper Jacobsson, J.-P. Correa-Baena, M. Pazoki, M. Saliba, K. Schenk, M. Grätzel, A. Hagfeldt, *Energy Environ. Sci.* **2016**, *9*, 1706; b) O. Almora, D. Baran, G. C. Bazan, C. Berger, C. I. Cabrera, K. R. Catchpole, S. Erten-Ela, F. Guo, J. Hauch, A. W. Y. Ho-Baillie, T. J. Jacobsson, R. A. J. Janssen, T. Kirchartz, N. Kopidakis, Y. Li, M. A. Loi, R. R. Lunt, X. Mathew, M. D. McGehee, J. Min, D. B. Mitzi, M. K. Nazeeruddin, J. Nelson, A. F. Nogueira, U. W. Paetzold, N. G. Park, B. P. Rand, U. Rau, H. J. Snaith, E. Unger, et al., *Adv. Energy Mater.* **2021**, *11*, 2102526.
- [9] <https://www.nrel.gov/pv/cell-efficiency.html> (accessed: October 2022).
- [10] D. Han, M. Imran, M. Zhang, S. Chang, X.-G. Wu, X. Zhang, J. Tang, M. Wang, S. Ali, X. Li, G. Yu, J. Han, L. Wang, B. Zou, H. Zhong, *ACS Nano* **2018**, *12*, 8808.
- [11] M. Auf der Maur, F. Matteocci, A. Di Carlo, M. Testa, *Appl. Phys. Lett.* **2022**, *120*, 113505.
- [12] a) J. H. Heo, D. H. Song, S. H. Im, *Adv. Mater.* **2014**, *26*, 8179; b) J. Duan, Y. Zhao, X. Yang, Y. Wang, B. He, Q. Tang, *Adv. Energy Mater.* **2018**, *8*, 1802346; c) Y. Zhao, H. Xu, Y. Wang, X. Yang, J. Duan, Q. Tang, *J. Power Sources* **2019**, *440*, 227151.
- [13] S. Rühle, *Sol. Energy* **2016**, *130*, 139.
- [14] R. K. Misra, S. Aharon, B. Li, D. Mogilyansky, I. Visoly-Fisher, L. Etgar, E. A. Katz, *J. Phys. Chem. Lett.* **2015**, *6*, 326.
- [15] J. A. Schwenzler, T. Hellmann, B. A. Nejang, H. Hu, T. Abzieher, F. Schackmar, I. M. Hossain, P. Fassel, T. Mayer, W. Jaegermann, U. Lemmer, U. W. Paetzold, *ACS Appl. Mater. Interfaces* **2021**, *13*, 15292.
- [16] B. Brunetti, C. Cavallo, A. Ciccio, G. Gigli, A. Latini, *Sci. Rep.* **2016**, *6*, 31896.
- [17] D. Di Girolamo, M. I. Dar, D. Dini, L. Gontrani, R. Caminiti, A. Mattoni, M. Graetzel, S. Meloni, *J. Mater. Chem. A* **2019**, *7*, 12292.
- [18] A. A. Zhumekenov, M. I. Saidaminov, M. A. Haque, E. Alarousu, S. P. Sarmah, B. Murali, I. Dursun, X.-H. Miao, A. L. Abdelhady, T. Wu, O. F. Mohammed, O. M. Bakr, *ACS Energy Lett.* **2016**, *1*, 32.
- [19] Y. Zhang, Y. Liang, Y. Wang, F. Guo, L. Sun, D. Xu, *ACS Energy Lett.* **2018**, *3*, 1808.



- [20] A. A. Sutanto, V. I. E. Queloz, I. Garcia-Benito, K. Laasonen, B. Smit, M. K. Nazeeruddin, O. A. Syzgantseva, G. Grancini, *APL Mater.* **2019**, *7*, 041110.
- [21] Y. L. Hangkai Ying, Y. Dou, J. Zhang, Z. Wu, Q. Zhang, Y.-B. Cheng, J. Zhong, *Front. Optoelectron.* **2020**, *13*, 272.
- [22] S. B. Shivarudraiah, N. Tewari, M. Ng, C. H. A. Li, D. Chen, J. E. Halpert, *ACS Appl. Mater. Interfaces* **2021**, *13*, 37223.
- [23] F. Matteocci, L. Vesce, F. U. Kosasih, L. A. Castriotta, S. Cacovich, A. L. Palma, G. Divitini, C. Ducati, A. Di Carlo, *ACS Appl. Mater. Interfaces* **2019**, *11*, 25195.
- [24] F. Ye, W. Tang, F. Xie, M. Yin, J. He, Y. Wang, H. Chen, Y. Qiang, X. Yang, L. Han, *Adv. Mater.* **2017**, *29*, 1701440.
- [25] B. Taheri, E. Calabrò, F. Matteocci, D. Di Girolamo, G. Cardone, A. Liscio, A. Di Carlo, F. Brunetti, *Energy Technol.* **2020**, *8*, 1901284.
- [26] a) E. Calabrò, F. Matteocci, B. Paci, L. Cinà, L. Vesce, J. Barichello, A. Generosi, A. Reale, A. Di Carlo, *ACS Appl. Mater. Interfaces* **2020**, *12*, 32536; b) Q. Jiang, X. Zhang, J. You, *Small* **2018**, *14*, 1801154; c) H. Wang, J. Yuan, J. Xi, J. Du, J. Tian, *J. Phys. Chem. Lett.* **2021**, *12*, 9142.
- [27] Y. Wang, L. Duan, M. Zhang, Z. Hameiri, X. Liu, Y. Bai, X. Hao, *Sol. RRL* **2022**, *6*, 2200234.
- [28] F. Hou, B. Shi, T. Li, C. Xin, Y. Ding, C. Wei, G. Wang, Y. Li, Y. Zhao, X. Zhang, *ACS Appl. Mater. Interfaces* **2019**, *11*, 25218.
- [29] E. Lamanna, F. Matteocci, E. Calabrò, L. Serenelli, E. Salza, L. Martini, F. Menchini, M. Izzi, A. Agresti, S. Pescetelli, S. Bellani, A. E. Del Río Castillo, F. Bonaccorso, M. Tucci, A. Di Carlo, *Joule* **2020**, *4*, 865.
- [30] a) T. Bu, X. Liu, Y. Zhou, J. Yi, X. Huang, L. Luo, J. Xiao, Z. Ku, Y. Peng, F. Huang, Y.-B. Cheng, J. Zhong, *Energy Environ. Sci.* **2017**, *10*, 2509; b) D. Chen, S. Pang, L. Zhou, X. Li, A. Su, W. Zhu, J. Chang, J. Zhang, C. Zhang, Y. Hao, *J. Mater. Chem. A* **2019**, *7*, 15156.
- [31] H. Wang, H. A. Dewi, T. M. Koh, A. Bruno, S. Mhaisalkar, N. Mathews, *ACS Appl. Mater. Interfaces* **2020**, *12*, 484.
- [32] M. A. A. Mamun, P. Dargusch, D. Wadley, N. A. Zulkarnain, A. A. Aziz, *Renewable Sustainable Energy Rev.* **2022**, *161*, 112351.
- [33] A. Perumal, S. Shendre, M. Li, Y. K. E. Tay, V. K. Sharma, S. Chen, Z. Wei, Q. Liu, Y. Gao, P. J. S. Buenconsejo, S. T. Tan, C. L. Gan, Q. Xiong, T. C. Sum, H. V. Demir, *Sci. Rep.* **2016**, *6*, 36733.
- [34] L. A. Muscarella, E. M. Hutter, S. Sanchez, C. D. Dieleman, T. J. Savenije, A. Hagfeldt, M. Saliba, B. Ehrler, *J. Phys. Chem. Lett.* **2019**, *10*, 6010.
- [35] a) K. Huang, Y. Peng, Y. Gao, J. Shi, H. Li, X. Mo, H. Huang, Y. Gao, L. Ding, J. Yang, *Adv. Energy Mater.* **2019**, *9*, 1901419; b) E. H. Anaraki, A. Kermanpur, L. Steier, K. Domanski, T. Matsui, W. Tress, M. Saliba, A. Abate, M. Grätzel, A. Hagfeldt, J.-P. Correa-Baena, *Energy Environ. Sci.* **2016**, *9*, 3128.
- [36] G. S. Han, J. Kim, S. Bae, S. Han, Y. J. Kim, O. Y. Gong, P. Lee, M. J. Ko, H. S. Jung, *ACS Energy Lett.* **2019**, *4*, 1845.
- [37] S. Pang, X. Li, H. Dong, D. Chen, W. Zhu, J. Chang, Z. Lin, H. Xi, J. Zhang, C. Zhang, Y. Hao, *ACS Appl. Mater. Interfaces* **2018**, *10*, 12731.
- [38] M. V. Khenkin, E. A. Katz, A. Abate, G. Bardizza, J. J. Berry, C. Brabec, F. Brunetti, V. Bulović, Q. Burlingame, A. Di Carlo, R. Cheacharoen, Y.-B. Cheng, A. Colmann, S. Cros, K. Domanski, M. Dusza, C. J. Fell, S. R. Forrest, Y. Galagan, D. Di Girolamo, M. Grätzel, A. Hagfeldt, E. von Hauff, H. Hoppe, J. Kettle, H. Köbler, M. S. Leite, S. Liu, Y.-L. Loo, J. M. Luther, et al., *Nature Energy* **2020**, *5*, 35.
- [39] a) A. Dasgupta, S. Mahesh, P. Caprioglio, Y.-H. Lin, K.-A. Zaininger, R. D. J. Oliver, P. Holzhey, S. Zhou, M. M. McCarthy, J. A. Smith, M. Frenzel, M. G. Christoforo, J. M. Ball, B. Wenger, H. J. Snaith, *ACS Energy Lett.* **2022**, *7*, 2311; b) S. Cacovich, G. Vidon, M. Degani, M. Legrand, L. Gouda, J.-B. Puel, Y. Vaynzof, J.-F. Guillemoles, D. Ory, G. Grancini, *Nat. Commun.* **2022**, *13*, 2868.
- [40] C. M. Wolff, P. Caprioglio, M. Stolterfoht, D. Neher, *Adv. Mater.* **2019**, *31*, 1902762.